Flow Control of an Oblique Shock Wave Reflection with Micro-ramp Vortex Generators: Effects of Location and Size

R.H.M. Giepman, F.F.J. Schrijer and B.W. van Oudheusden
Aerospace Engineering Department, Delft University of Technology,
Kluyverweg 1, 2629HS Delft, The Netherlands

Abstract

The effects of micro-ramp height and location on a shock induced separation bubble were quantified using planar particle image velocimetry measurements. Conditional averaging was used to show that the amount of separation is related to the momentum flux in the near-wall region ($< 0.5\delta$) of the incoming boundary layer. The momentum flux added to this region scales linearly with micro-ramp height and larger micro-ramps are shown to be more effective in stabilizing the interaction. Full boundary layer mixing is attained 5.7δ downstream of the micro-ramp and this forms a lower limit on the required distance between micro-ramp and reflected shock foot.

1. Introduction

Shock wave boundary layer interactions are prevalent in many aerospace applications that involve transonic or supersonic flows. These interactions appear on transonic wings, compressor blades of jet engines, and supersonic inlets. They still pose a problem of technical relevance due to their associated unsteady pressure and heat loads [1]. Furthermore, when regarded in the framework of inlets, it is well-known that large areas of separated flow may significantly reduce the engine's efficiency [2]. The shock unsteadiness associated with such an interaction can result in large structural loads and in a worst-case scenario cause the inlet to unstart. Flow control strategies are therefore being investigated to reduce the amount of separation and shock unsteadiness by stabilizing the incoming boundary layer.

A well-known solution is to bleed off the low-momentum portion of the boundary layer, which results in a fuller and more stable boundary layer profile. The mass flow removed from the inlet (about 2% of the capture inlet mass flow [3]) is typically not reinjected elsewhere in the engine and is vented overboard. This requires the frontal area of the engine to be increased, which increases both the engine's drag and weight.

Micro-ramp vortex generators provide a promising alternative to boundary layer bleed. Their typical height is about 50% of the boundary layer thickness and their effectiveness comes from the two counter-rotating vortices it introduces in the flow [4]. These vortices transport high-momentum fluid towards the wall, thus creating a fuller boundary layer profile, allowing the flow to pass through the shock system with less separation [5–8]. Anderson et al. [9] used Reynolds Averaged Navier Stokes (RANS) simulations to show that micro-ramps can reduce the incompressible shape factor of the incoming boundary layer to the same level as obtainable with boundary layer bleed.

A lower shape factor and a reduced amount of separation were observed in the surface pressure and laser doppler anemometry measurements of Babinsky et al. [8]. The amount of separation was not measured directly, but is expected to be related to the size of the interaction region. Furthermore, surface oil flow measurements showed that separation is not completely removed, but instead broken up in a cellular structure. The interaction region and separation bubble were investigated in more detail by Blinde et al. [10], who carried out Stereo Particle Image Velocimetry measurements in planes parallel to the wall. Compared to a flow without micro-ramps, the separation probability was reduced by 20-30% and the shock oscillation amplitude by 20%.

A shock wave boundary layer interaction controlled by micro-ramps poses significant challenges for numerical flow simulations. The work of Lee [11] showed that RANS computations are not very well suited for these kind of problems and deliver results that deviate significantly from experimental data. Large Eddy Simulations (LES) simulations on the other hand produce results that are much closer to the experimental evidence. The LES simulations indicate, amongst other findings, that smaller micro-ramps result in an improved pressure recovery over the shock and less separation. These observations do not match the results of Babinsky [8], who measured the opposite trend.

To successfully apply micro-ramps in a supersonic inlet it is of critical importance to understand how the size and position of the micro-ramp affect the separation probability and shock unsteadiness. A parametric study was

therefore carried out, focussing on the quantification of these parameters. Planar Particle Image Velocimetry (2C-PIV) measurements were carried out to instantaneously capture the separation bubble and inflow conditions. The results of the parametric study are interpreted by analysing the effects of the micro-ramp on the boundary layer entering the interaction. Conditional averaging is then used to find relations between the incoming boundary layer profile and the behaviour of the interaction region.

2. Experimental arrangement

2.1 Flow facility

The experiments were carried out in the ST-15 blow-down supersonic wind tunnel of the Delft University of Technology. The test section measures 150x150 mm^2 and the tunnel is operated at a Mach number of 2, a total pressure p_0 of 3.2 bars and a total temperature T_0 of 290 K. This results in a freestream velocity U_∞ of 524 m/s and a unit Reynolds number of 42.2 million. The incident shock wave is created by a nearly full-span 12 degree shock generator. The shock generator is designed such that the expansion fan coming from its shoulder does not interfere with the shock wave boundary layer interaction (see Fig.2).

The boundary layer on the bottom wall of the tunnel is used for all the experiments in this paper. It develops along a smooth surface for approximately 1 m under nearly adiabatic conditions and reaches a thickness δ_{99} = 5.2 mm in the test section. The properties of the undisturbed boundary layer were measured by means of a dedicated PIV experiment at high resolution. A spatial resolution of 59 pixels/mm was used and the laser pulse separation was set to 1 µs, resulting in a freestream particle displacement of 31 pixels. The incompressible displacement thickness δ^* is determined to be 0.63 mm, the momentum thickness θ = 0.52 mm and the incompressible shape factor H_{inc} = 1.23. The Reynolds number based on the incompressible momentum thickness equals: $Re_\theta = \rho_\infty U_\infty \theta/\mu_\infty = 21.8 \times 10^3$, with μ_∞ being the dynamic viscosity of the freestream.

By using the Van Driest II transformation in combination with the Crocco-Busemann relation (recovery factor r = 0.89), the skin friction coefficient c_f and friction velocity u_τ are determined from a log-law fit which yields, 1.9×10^{-3} and 20.8 m/s, respectively. The experimental conditions and boundary layer properties are summarized in Table 1.

Table 1: Experimental conditions and undisturbed boundary layer properties

Parameter	Quantity	Parameter	Quantity
M_∞	2.0	θ (mm)	0.52
U_∞ (m/s)	524	H_{inc}	1.23
p_0 (N/m^2)	3.2×10^5	u_τ (m/s)	20.8
T_0 (K)	290	c_f	1.9×10^{-3}
δ_{99} (mm)	5.2	Re (1/m)	42.2×10^6
δ^* (mm)	0.63	Re_θ	21.8×10^3

2.2 Micro-ramps configuration and experimental matrices

The micro-ramps used in this study are based on the recommendations of Anderson [9] for minimizing H_{inc} downstream of the micro-ramp. The dimensions of this micro-ramp are presented in Fig.1 and are normalized with the micro-ramp height h.

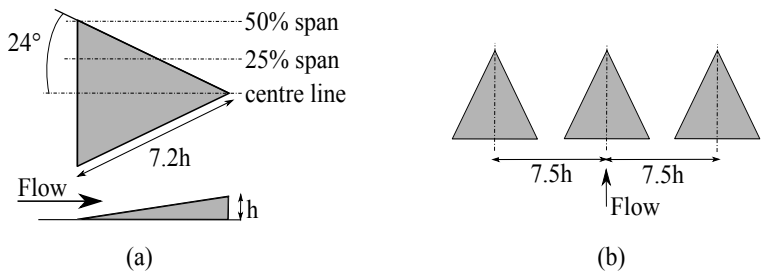

Figure 1: Dimensions of a single micro-ramp (a) and an array of three ramps (b)

Table 2 provides an experimental matrix for the parametric study that was carried out. Three different micro-ramp heights were investigated in this study, namely 2, 3 and 4 mm (set A-C), which were mounted at a range of distances d: the distance between the trailing edge of the micro-ramp and the inviscid impingement point of the incident shock wave. All the measurements in set A-C were carried out on the centreline of the micro-ramp. Set D considers the flow behaviour at two off-centre location, namely 25 and 50% span (see Fig.1(a)). In set E, three 4 mm micro-ramps were mounted next to each other in the tunnel (see Fig.1(b)). The spacing s between the centre lines of the micro-ramps equals $7.5h$ = 30 mm, which is the value recommended by Anderson [9] and the one commonly used by other researchers in this field [8, 10, 11]. Finally, in set F the undisturbed shock wave boundary layer interaction is investigated, which will serve as a reference for all other cases.

For all the configurations investigated in this parametric study, 150 image pairs were recorded. For statistical purposes, the measurements on two configurations (see Table 3) were repeated and two datasets of 500 image pairs were obtained.

Table 2: Experimental matrix for the parametric study

	Number of ramps	Spacing s	Height h	Distance d	Plane
A	1	-	2 mm	8.1, 10.4, 13.8, 17.3 & 20.8δ	Centre
B	1	-	3 mm	10.4, 13.8, 17.3 & 20.8δ	Centre
C	1	-	4 mm	10.4, 13.8, 17.3 & 20.8δ	Centre
D	1	-	4 mm	17.3δ	25% span, 50% span
E	3	7.5h	4 mm	17.3δ	Centre, 25% span, 50% span
F	Clean configuration - No micro-ramp				

Table 3: Experimental matrix for the overview measurements

	Number of ramps	Spacing s	Height h	Distance d	Plane
G	1	-	4 mm	17.3δ	Centre
H	Clean configuration - No micro-ramp				

2.3 PIV arrangement

Planar PIV measurements were carried out to capture the instantaneous flow field downstream of the micro-ramp and inside the interaction region. For the parametric study (Table 2) two 16 MP Lavision Imager Pro LX cameras were used simultaneously. One of the cameras was zoomed in on the interaction region and the other was focused on the inflow into the interaction. An overlap of 20 mm is provided for allowing the datasets to be combined properly (See Fig.2).

On the 'interaction' camera a 105 mm Nikkor objective was used with $f_\#$ set to 5.6. Cropping and binning (2x2) were applied to speed up data acquisition (see Table 4). This resulted in a Field of View (FOV) of 50x20 mm and 48 pixels/mm for the interaction camera. On the 'inflow' camera a 60 mm Nikkor objective was used with $f_\#$ also set to 5.6 and the image was cropped to fit the laser sheet, which resulted in a FOV of 95x20 mm and 35 pixels/mm. However, due to strong laser reflections coming from the micro-ramp, it was not possible to use the full FOV and measurements could not be carried out within 10 mm of the ramp. For the 'overview' measurements of Table 3, only one of the cameras was used. To speed up the acquisition process, the camera was zoomed out and cropped in the wall normal direction. A 60 mm Nikkor objective was used with $f_\#$ set to 5.6. This resulted in a FOV of 80x13 mm and a digital resolution of 25 pixels/mm.

Table 4: Viewing configuration for the PIV measurements

Configuration	FOV		Resolution		Particle displacement
	mm	pixels	µm/pixel	mm/vector	pixels
Interaction	50×20	2416×967	21	0.16	25
Inflow	95×20	3291×693	29	0.17	18
Overview	80×13	1955×333	41	0.25	13

Illumination was provided by a Quantel Evergreen double-pulsed Nd:YAG laser with a pulse energy of 200 mJ and a pulse duration of <10 ns. A pulse separation of 1 µs was used, resulting in particle displacements of 25, 18 and 13 pixels for the interaction, inflow and overview field of view, respectively. The flow was seeded with DEHS particles, having a nominal diameter of 1 µm and a relaxation time τ of 2 µs, as determined by Ragni et al. [12]. This translates into a Stokes number of $\tau U_\infty/\delta = 0.2$, which according to Samimy [13] can result in slip velocities of maximal $0.02U_\infty$.

Davis 7.4 was used for data acquisition and Davis 8.1 for processing the data. As a pre-processing step the particle intensity was normalized using a min/max filter. A multi-pass cross-correlation approach was used with final interrogation windows of 32x32 pixels and 75% overlap for the interaction camera. For the inflow and overview camera 24x24 windows with 75% overlap were used. The resulting vector pitches are summarized in Table 4. Spurious vectors were removed by means of the universal outlier detection [14] approach implemented in Davis.

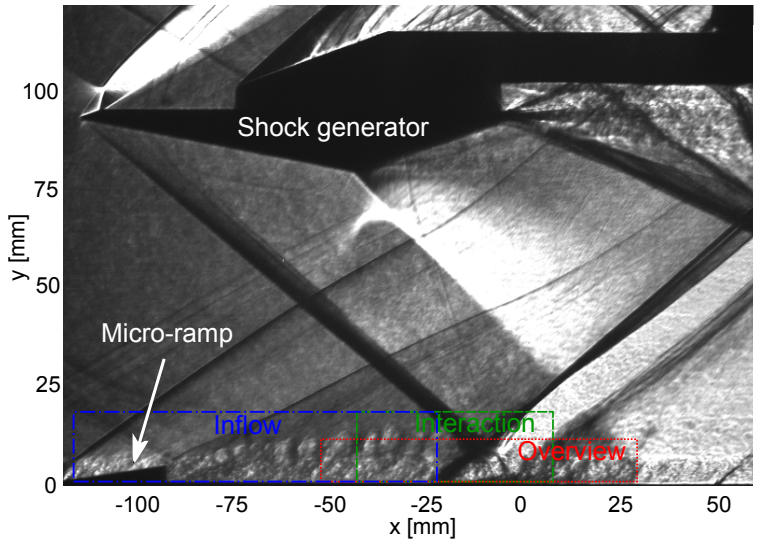

Figure 2: Spark-light Schlieren visualization of the tunnel setup, overlayed are the fields of views used for the different camera configuration.

2.4 Uncertainty analysis

The measurements that were carried out are subject to uncertainties introduced by the limited sample size, the PIV measurements technique and micro-ramp positioning errors.

For the parametric study, 150 image pairs were recorded per case. The slowest rate of convergence was experienced in the region of the separation bubble, in this region the uncertainties on $\bar{u}$, u' and A_{sep} are estimated to be 0.48%, 0.94% and 0.69%, respectively. A_{sep} is the average separated area, an important parameter that will be introduced in section 3.2 to quantify the amount of separation per test case.

In the cross-correlation procedure, the location of the peak can only be determined with a finite accuracy of ~0.1 pixel. As a consequence, the instantaneous velocities measured are expected to be off by ~0.4% for the interaction field of view and ~0.55% for the inflow field of view.

The issue of particle slip has already been discussed in the previous section and for the DEHS particles used, slip velocities of <2% of the freestream velocity are expected. The effect of particle slip is most pronounced in regions where the particles are subjected to strong velocity gradient, for instance when passing a shock wave or inside vortices.

The micro-ramps were mounted in the tunnel by hand and although this was done with great precision, small positioning errors with respect to the laser sheet cannot be avoided. An offset of for instance 0.5 mm will significantly affect the velocity field that is measured, because the streamwise vortices that are responsible for the mixing process are of the same scale [15]. Even if the micro-ramp is perfectly aligned with the laser sheet, results will still be averaged due to the laser sheet thickness of approximately 1 mm. To investigate the sensitivity of the solution, several measurements were repeated and the uncertainty in the average separated area is expected to be 10-25%.

All the uncertainty parameters discussed are presented in Table 5 together with the values for the overview field of view. For the overview field of view 500 proper image pairs were recorded and consequently the statistical errors are smaller than for the parametric study.

Table 5: Uncertainty analysis

Parameter	Parametric study (N = 150)	Overview measurements (N = 500)
Statistical uncertainty		
• Average velocity $\epsilon_{\bar{u}}/U_\infty$	0.48%	0.13%
• Velocity fluctuations $\epsilon_{u'}/U_\infty$	0.94%	0.47%
• Average separated area $\epsilon_{A_{sep}}/A_{sep}$	0.69%	0.26%
Cross correlation uncertainty ϵ_{CC}	0.1 pixel	0.1 pixel
Instantaneous velocity $\epsilon_{u(\epsilon_{CC})}/U_\infty$	0.4 - 0.55%	0.78%
Particle slip ϵ_τ/U_∞	<2%	<2%
Repeatability $\epsilon_{\Delta A_{sep}}/A_{sep}$	10 - 25%	

3. Results

3.1 Assessment of the undisturbed boundary layer

This study relies heavily upon PIV measurements of the boundary layer, so it is important to validate these measurements against well-known reference solutions. Fig.3a and (b) present the results of a PIV measurement of the undisturbed turbulent boundary layer, without a micro-ramp or shock generator mounted in the tunnel.

Fig.3a shows the mean velocity profile in terms of the inner variables $u^+ = u_{eq}/u_\tau$ and $y^+ = yu_\tau/\mu_w$. Here u_τ presents the friction velocity, μ_w the kinematic viscosity at the wall and u_{eq} the Van Driest effective velocity. The latter is obtained by applying the Van Driest II transformation in combination with the Crocco-Busemann relation (recovery factor r = 0.89) to the boundary layer profile. From Fig.3a it is clear that an excellent agreement between the boundary layer profile and the log law is obtained in the region from y^+ = 200 to y^+ = 900, for a friction velocity u_τ of 20.8 m/s. For $y^+ > 900$ a wake component can be distinguished, which can be described in terms of Coles' law of the wake [16]. Coles' wake parameter Π is calculated to be 0.54, which falls within the range found in the study of Fernholz and Finley [17]. They showed that for flat-plates with $1.7 < M < 10.3$ and $Re_\theta > 2000$, Coles' wake parameter equals: $\Pi = 0.55 \pm 0.05$.

Fig.3b shows the fluctuations in the boundary layer profile in both streamwise and wall-normal direction. In order to allow a direct comparison with the classical incompressible data of Klebanoff [18], the fluctuations are normalized with respect to the friction velocity and scaled with $\sqrt{\rho/\rho_w}$ (Morkovin scaling). The density ratio is calculated from the mean velocity profile by using the adiabatic Crocco-Busemann relation with a recovery factor r of 0.89. Besides Klebanoff's results also the results from the tomographic PIV study of Humble et al. [19] and the Hot Wire Anemometry (HWA) study of Elena et al. [20] are shown in the figure. The measurements reported in this study are in good agreement with the reference cases and therefore substantiate the validity of the experimental approach.

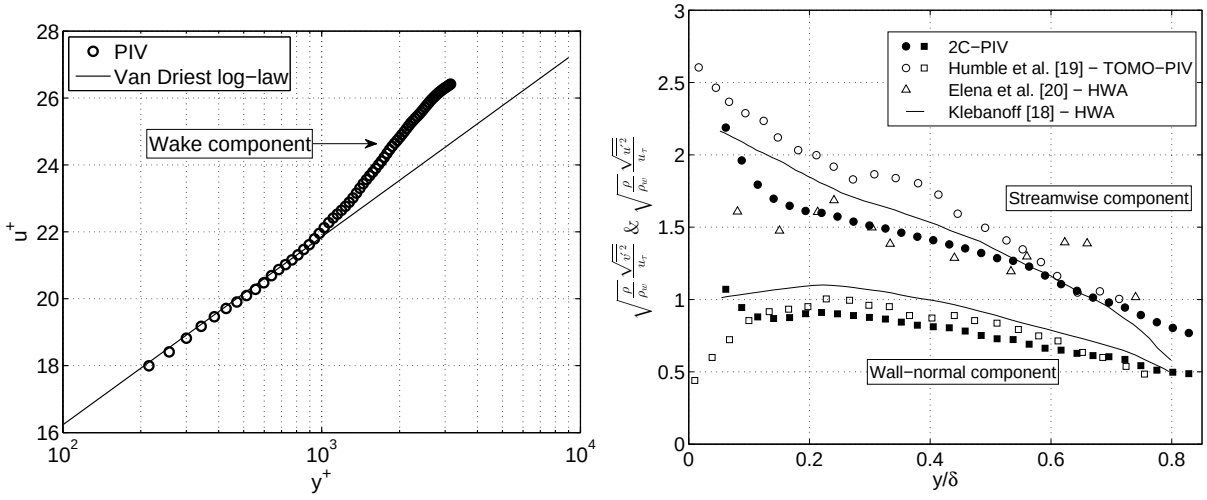

(a) Log law fit

(b) Velocity fluctuations in Morkovin scaling

Figure 3: Assessment of the undisturbed boundary layer

3.2 Effects of the micro-ramp on the interaction region

Before zooming in on the interaction region it is useful to first consider the global features of the flow in the Schlieren visualization of Fig.2. A 12 degree nearly full-span shock generator is used to create the incident shock wave, which by definition impinges on the wall at $x = 0$ mm. The reflected shock is formed approximately 25 mm upstream. For this measurement a 4 mm micro-ramp was placed 90 mm (17.3δ) upstream of the incident shock's impingement point. The micro-ramp is completely embedded in the boundary layer and both the leading edge shock and the lip shock (terminating the expansion wave over the micro-ramp's corner) are clearly visible. The boundary layer is growing in thickness after passing the micro-ramp.

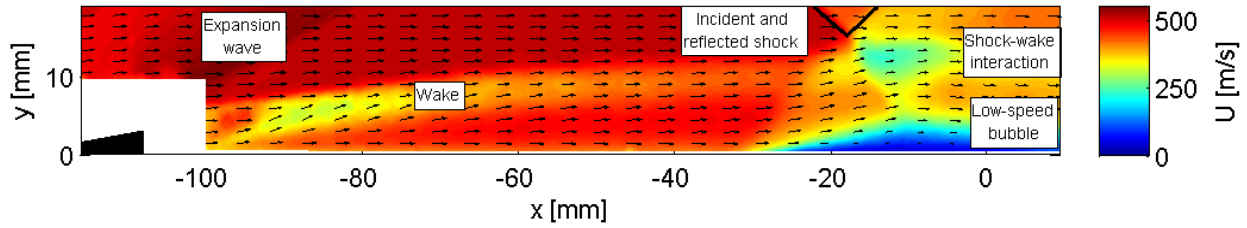

Figure 4: An overview of the flow field from micro-ramp until interaction region. For this measurement a 3 mm micro-ramp was placed at $x = -20.8\delta$. Presented is the u-component of the velocity field.

By combining the inflow and interaction field of view, the velocity field from micro-ramp until interaction can be constructed. In Fig.4 the u-velocity component is presented for the case of a 3 mm micro-ramp at $x = -108$ mm (20.8δ). For this case, the measurement plane coincides with the symmetry plane of the ramp. The region close to the micro-ramp is blanked out, because reflections were too strong to allow a proper measurement. Behind the ramp a wake can be distinguished which lifts away from the surface and weakens when moving downstream. Around $x = -20$ mm the wake interacts with the shock system and a low-velocity pocket is formed. Another important feature of Fig.4 is the low-speed bubble formed at the wall, which is caused by the strong adverse pressure gradient imposed on the incoming boundary layer by the reflected shock wave. Both the reflected shock wave and the separation bubble are behaving in an unsteady manner. Whereas on average there is no separation taking place for this particular case of micro-ramp position and height, instantaneously this can still occur (the instantaneous snapshots in Fig.7 clearly show this).

The interaction region is the focal point of this section and Fig.5 shows the difference in flow topology between a case with ($h = 4$ mm & $d = 17.3\delta$) and without micro-ramp. Fig.5(a) and (b) compare the u-component of the average velocity field and Fig.5(c) and (d) compare the turbulence intensities. The solid black line presents the dividing streamline, which divides the separation bubble from the outer flow, while the dotted black line is the sonic line. Note that on average there is no separation taking place for the case with a micro-ramp. The weaker separation bubble results in a shear layer with smaller velocity gradients. As a consequence the production of vorticity is reduced and lower turbulence levels are recorded in this region of the flow. The turbulence intensities recorded in the centre of the shear layer are approximately 15% smaller for the case with a micro-ramp. Lower turbulence levels are, however, also recorded downstream of the interaction, within the recovering boundary layer. Finally, notice that the highest values for the turbulence intensity are recorded in the region enclosed by the dividing streamline and the sonic line, an observation that was also made in the work of Souverein [21].

Although this study focuses on the behaviour of the interaction region in the symmetry plane of the micro-ramp, it is important to emphasize that its efficiency decreases when moving to off-centre planes. Fig.6 presents measurements in different spanwise planes and reveals the strongly three-dimensional effect of the micro ramp on the interaction. Three slices are shown, at the centre line, 25% span and 50% span (see Fig.1 for reference). As the measurement plane is moved away from the centre, the separated region increases. At $z/\delta = 2.3$ (50% span), the mean flow field and size of the separated region is similar to that of a flow without a micro-ramp (exact values are presented in Fig.9a). The micro-ramp therefore does not remove separation completely, but instead creates a spanwise modulation in the bubble. A similar observation was also made in the work of Babinsky and Pitt Ford [8], where oil-flow visualizations were used to show that the effects of the micro-ramp do not reach far beyond its span and that attached flow is only observed within the centreline region.

The unsteady behaviour of the separation bubble is illustrated in Fig.7, showing three snapshots of the interaction region. For this measurement a 4 mm micro-ramp was located at $x/\delta = 17.3$. In Fig.7(a) the flow is attached down to

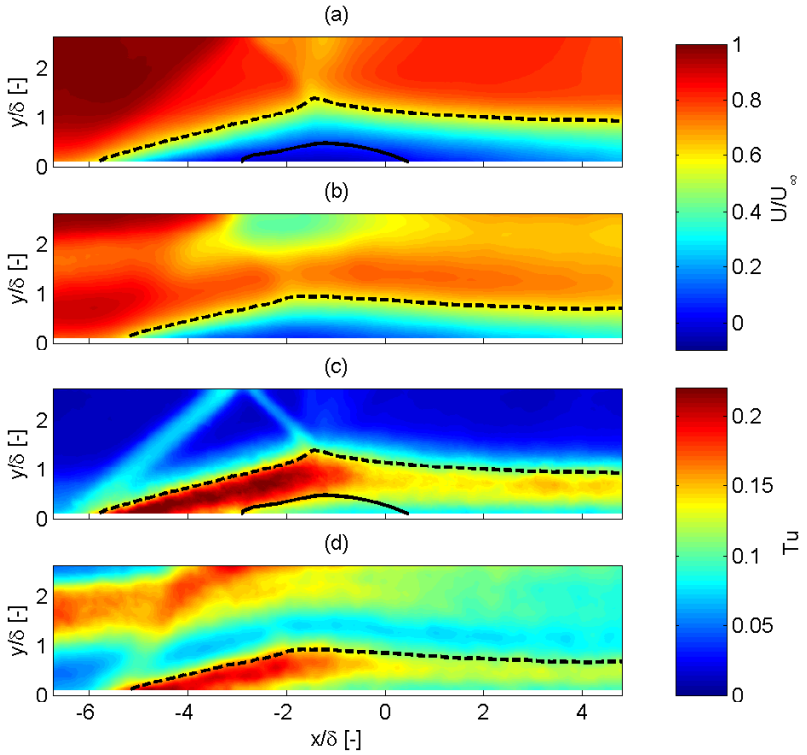

Figure 5: The interaction region for a case with (h = 4 mm and $d = 17.3\delta$) and without micro-ramp. (a) U/U_∞ without and (b) with a micro-ramp (c) Turbulence intensity $Tu = \sqrt{u'^2 + v'^2}/U_\infty$ without and (d) with a micro-ramp.

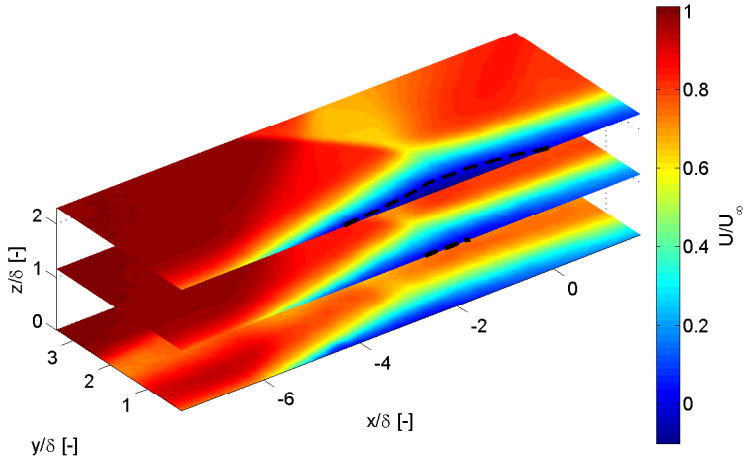

Figure 6: Normalized streamwise velocity distribution in the interaction region, for a 4 mm micro-ramp located at $d = 17.3\delta$. The three planes correspond to a cut through the centerline ($z = 0$), at 25% span ($z = 1.15\delta$) and 50% span ($z = 2.3\delta$). The dashed line presents the zero-velocity contour.

$y/\delta = 0.07$. Fig.7(b) shows a small separation bubble of approximately 6 mm^2 and Fig.7(c) indicates the presence of a large bubble of approximately 44 mm^2.

From the individual snapshots the separation probability P_{sep} can be obtained. The separation probability is defined as the probability that a certain point (x,y) shows reversed flow. So, if $P_{sep}(x, y)$ equals 50%, then half of the time the flow is reversed at (x, y) and half of the time it is attached. Fig.8 compares the separation probability with (a) and without a micro-ramp (b). Without a micro-ramp, flow reversal is observed in a region spanning the entire field of view, so approximately 9δ. By placing a 4 mm micro-ramp 17.3δ upstream of the interaction this is reduced

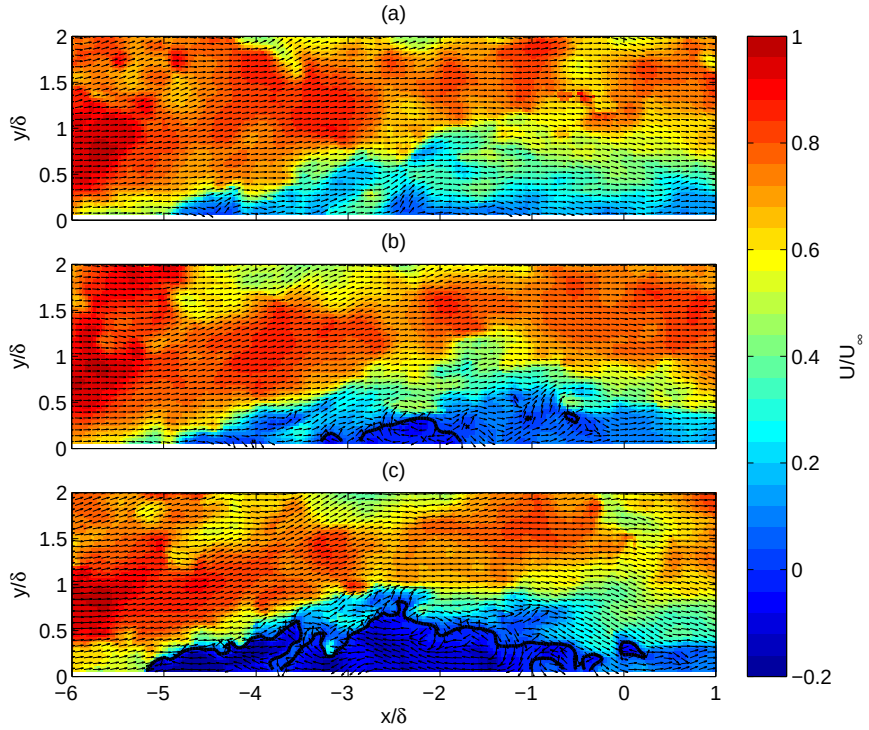

Figure 7: Three PIV snapshots of the low-speed bubble. For a 4 mm micro-ramp positioned at $x/\delta = -17.3$, measured along its centre line. The solid black line presents the zero-velocity contour. (a) No separation (b) Small separation bubble (c) Large separation bubble

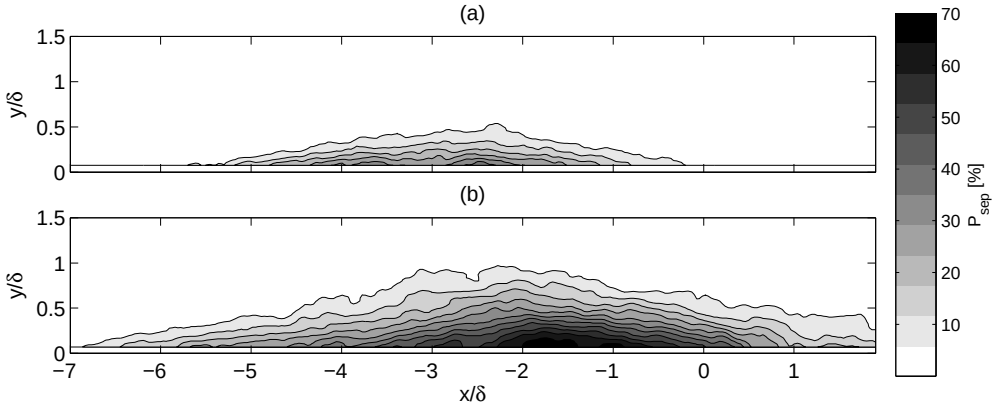

Figure 8: The separation probability P_{sep} with a micro-ramp ($h = 4$ mm, $d = 17.3\delta$) upstream of the interaction (a) and without a micro-ramp (b).

to 5.5δ. Also the probability of encountering reversed flow is reduced. Without a micro-ramp there are regions close to the wall that show flow reversal 75% of the time. With a micro-ramp this peak value has been reduced to 41%. By integrating the separation probability over the entire domain, the average separated area A_{sep} can be calculated. Without a micro-ramp A_{sep} equals 37.4 mm^2 and with a micro-ramp ($h = 4mm$ and $d = 17.3\delta$) it decreases to 8.1 mm^2.

The location and height of the micro-ramp have a pronounced effect on the behaviour of the interaction and the amount of reversed flow, therefore a parametric study has been carried out in which both parameters were investigated (See Table 2). The results of this study are summarized in the Figs.9a and (b), which show the average separated area and the shock unsteadiness, respectively. In Fig.9a A_{sep} is normalized with $A_{sep,clean} = 37.4$ mm^2, which is the average separated area present for a clean configuration without a micro-ramp. So, except for the case of a 4 mm micro-ramp, located at $x/\delta = 17.2$ and measured at 50% span, all cases show an improvement with respect to the clean configuration.

However, one of the configurations tested ($h = 4$ mm, $d = 10.4\delta$) is not presented in Fig.9a. For this specific case, the separation bubble that forms behind the micro-ramp [8] combines with the shock induced separation bubble. The

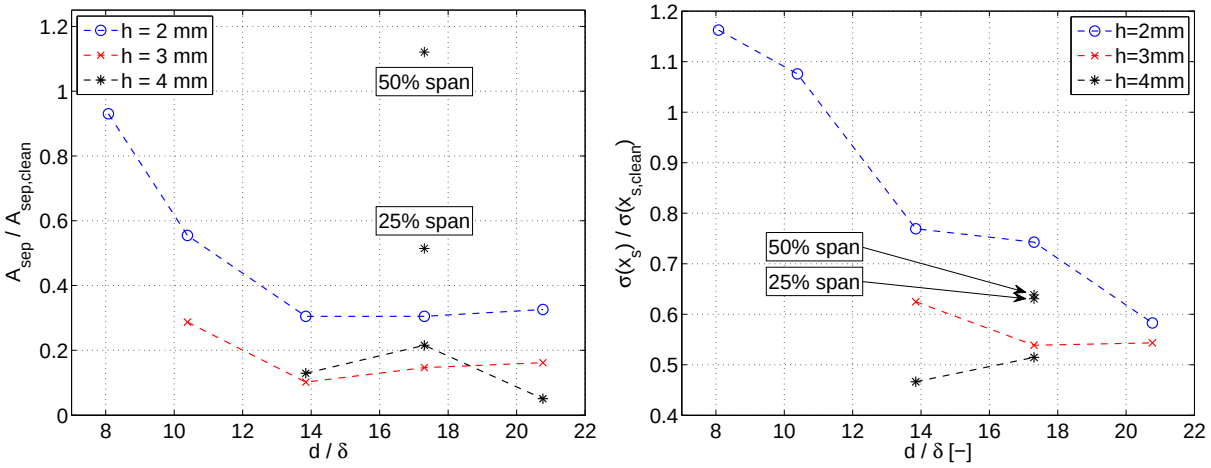

(a) Average separated area

(b) Reflected shock unsteadiness

Figure 9: Results of the parametric study

end result is a very large region of reversed flow that extends beyond the field of view, therefore making it impossible to give an accurate estimate for A_{sep}. The mean velocity field for this case is plotted in Fig.10 and the separated area (zero velocity contour) is compared to the clean configuration. Clearly, if the micro-ramp is placed too close to the interaction, the situation is worse than without a micro-ramp.

Also the performance of the 2 and 3 mm micro-ramp is reduced when placing it too close to the interaction. There is a distinct rise present in the average separated area when moving the ramp from $x = 13.8\delta$ to $x = 10.4\delta$. This rise can be explained in terms of the momentum flux that is added to the near-wall region of the boundary layer, a topic that will be discussed in section 3.3. Furthermore, notice in Fig.9a that the 3 and 4 mm micro-ramp perform better than the 2 mm ramp; the smallest average separated area is achieved with a 4 mm ramp located 20.8δ upstream of the interaction. For this particular case, the average separated area is reduced by a factor of 20 in the centreline region of the ramp.

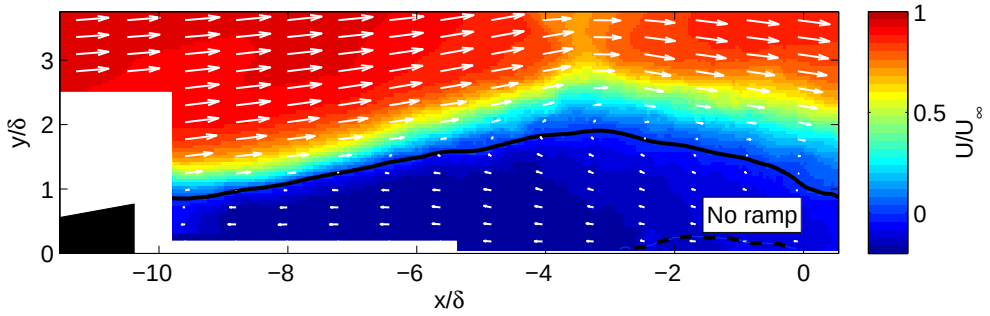

Figure 10: Mean velocity field for a 4 mm micro-ramp placed 10.4δ upstream of the incident shock. The solid black line presents the zero-velocity contour and as a reference the dashed line is inserted, which shows the zero-velocity contour for the clean configuration.

Since, the size of the separation bubble is correlated with the location of the reflected shock wave [22, 23], it is expected that by reducing the size of the separation bubble, the unsteadiness of the reflected shock wave is also reduced. The location of the reflected shock wave is determined by finding the maximum of dV/dx along the horizontal line $y = 3.5\delta$. The same procedure is repeated for the five rows of vectors above and below this line. After removing obvious outliers, the shock locations are used in a least squares fitting procedure. The linear fit that results is used to calculate the reflected shock location at $y = 3.5\delta$. This process is repeated for all the snapshots and the shock unsteadiness is then determined as the standard deviation σ of the list of shock locations x_s.

Without a micro-ramp the reflected shock wave unsteadiness equals $\sigma(x_{s,clean}) = 1.87$ mm. Fig.9b presents the reflected shock wave unsteadiness $\sigma(x_s)$ normalized by $\sigma(x_{s,clean})$ for the clean configuration. It was not possible to calculate the shock unsteadiness for all test cases, because for some cases ($h = 4$ mm, $d/\delta = 10.4$ & 20.8 and h=3 mm, $d/\delta = 10.7$) the wake coming from the micro-ramp and/or vortices being shed from the separation bubble were

obscuring the velocity gradient imposed by the shock wave. It was therefore not possible to accurately resolve the instantaneous location of the shock wave and no estimate of the shock unsteadiness can be given. The data points for a 2 mm micro-ramp show that shock unsteadiness is reduced when moving the ramp away from the interaction. Furthermore, the larger micro-ramps appear to be more effective in reducing the unsteady behaviour of the reflected shock wave. With a 4 mm ramp placed at $d/\delta = 13.9$ or 17.2, $\sigma(x_s)$ is approximately halved. Finally, note that the shock unsteadiness is not only reduced in the symmetry plane of the ramp, but also at 25 and 50% span reductions of, respectively, 37 and 36% are obtained. It is especially interesting to see that at 50% span, the micro-ramp still reduces the shock unsteadiness, whereas the average separated area at this location is known to increase by 12% compared to a case without micro-ramp. It seems that the effect of the micro-ramp on the reflected shock wave is less localized than its effect on the separation bubble.

3.3 Working principles

The development of the boundary layer profile behind a 3 mm micro-ramp is presented in Fig.11. Profiles are shown at four locations behind the ramp, with x_{MR} defined as the distance between the measurement location and the trailing edge of the ramp. As a reference also the undisturbed boundary layer profile is presented. As expected, the wake region becomes less intense when traveling downstream and lifts off from the surface. Furthermore, notice that momentum is added to the near-wall region of the boundary layer. In the following analysis, the wake region and the near-wall region are treated separately. Firstly, we discuss the wake region and in particular how wake intensity and location scale with micro-ramp height. Secondly, we treat the momentum increase in the near-wall region. Finally, conditional averaging is applied to show the effects of these two regions on the separation bubble.

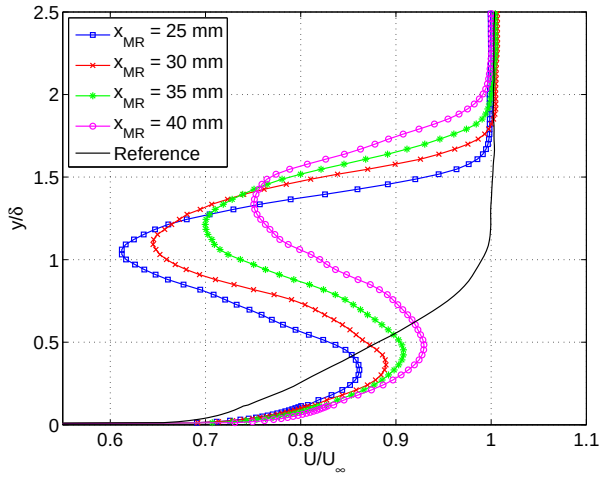

Figure 11: Development of the boundary layer behind a 3 mm micro-ramp.

Fig.12a shows the wake height y_{wake} as a function of the distance behind the micro-ramp x_{MR}. The wake height scales with the micro-ramp height h and the results from the 2, 3 and 4 mm, when scaled, collapse to one curve. The same observation has been made before by Ashill [4] in incompressible flows and by Babinsky [8] in a supersonic flow. As a reference also the fit from Babinsky is shown, which shows the same trend, but with an offset of approximately h for $x/h \geq 15$. This is probably due to the different operating conditions. Babinsky's experiments were carried out at a higher Mach number of 2.5, a higher Re_θ of 28.8×10^3 and a slightly thicker boundary layer of $\delta = 6$ mm.

Also the velocities in the centre of the wake U_{wake} scale with micro-ramp height. Fig.12b shows that the wake velocities for 2, 3 and 4 mm micro-ramps again collapse to one curve, when scaled with h.

In Fig.11 it was noticed that momentum is added to the near-wall region of the flow. To track the development of the added momentum flux downstream of the micro-ramp, the following metric is introduced:

$$E(x) = \int_0^{\frac{\delta_0}{2}} \frac{U^2 - U_{clean}^2}{U_\infty^2} dy \tag{1}$$

In which U_{clean} is the velocity field for the clean configuration without micro-ramp. The bounds are chosen from 0 to $0.5\delta_0$, because conditional averaging (see end of this section) revealed that the separation bubble is mostly sensitive to the momentum flux contained in this part of the boundary layer. A similar observation has been made in the work

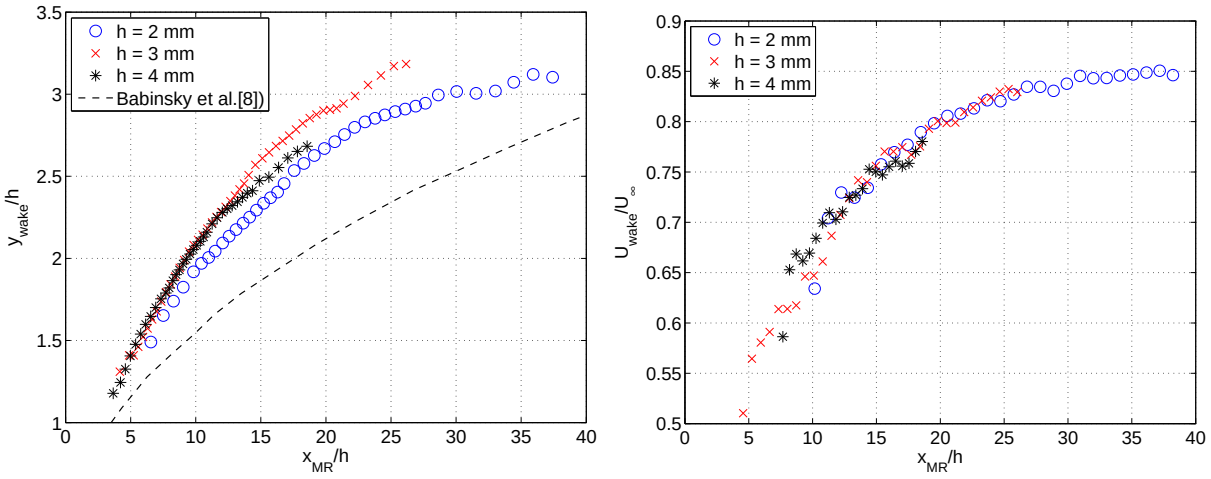

(a) Wake height

(b) Wake velocity

Figure 12: Location and intensity of the micro-ramps wake, normalized with the micro-ramp height

of Van Oudheusden et al. [23], who showed that the mean velocity in the lower half of the incoming velocity profile is correlated with the size of the separation bubble.

Fig.13 shows the development of the normalized added momentum flux E/h for a 2, 3 and 4 mm micro-ramp placed 17.3δ (x = -90 mm) upstream of the incident shock. The bottom x-axis shows the distance to the micro-ramp x_{MR} and the top axis the location with respect to the inviscid impingement point of the incident shock. Notice that all three datasets collapse to one curve. This implies that the added momentum flux scales linearly within the height of the micro-ramp. A possible explanation for this behaviour can be found in the work of Ashill et al. [4]. They investigated a range of different vortex generators (VGs) and noticed that vortex circulation scales linearly with VG height. This only holds true for non-dimensional VG heights of $h_e^+ = u_\tau h_e/\nu > 1400$, in which h_e is the effective height of the VG, which for forward wedges like the micro-ramp is the same as its physical height. A h_e^+ of 1400 translates to a micro-ramp height of 0.84 mm for our case. So, a linear increase in the vortex circulation may be expected when moving from a 2 to 3 and 4 mm micro-ramp. A vortex that is twice as strong should also be able to transport twice the amount of momentum flux down to the wall, which would explain why scaling E with h causes all the curves to collapse in Fig.13.

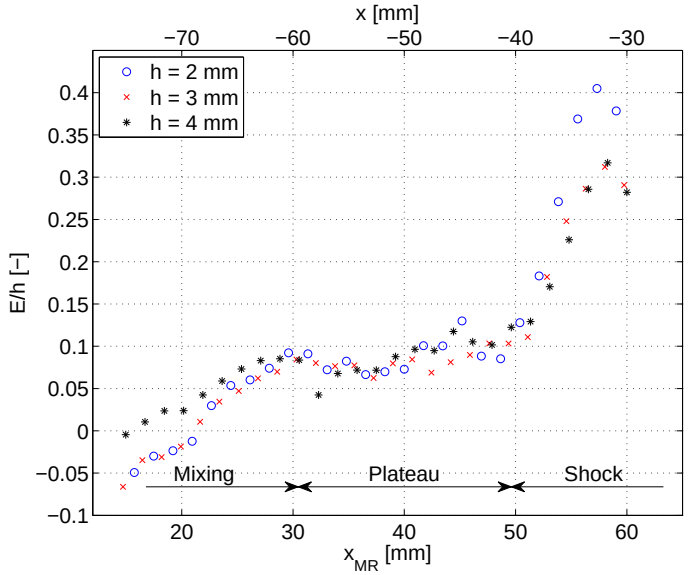

Figure 13: Development of the normalized added momentum flux E/h downstream of the micro-ramp

In Fig.13 three regions can be distinguished, a mixing region of 30 mm, a plateau of 20 mm and a shock region which becomes apparent at x = -40 mm. So, approximately 30 mm is needed to allow the streamwise vortices to transport high-momentum fluid towards the wall and low-momentum fluid away from the wall. Also a finite amount

of space is needed for the wake to lift off from the surface. After 30 mm E/h levels off and no more momentum flux is added to the near-wall region. There is a plateau of 20 mm = 3.8δ, which lasts until the reflected shock wave is encountered. So, if the micro-ramp would be shifted upstream by more than 3.8δ, then there is not enough time and space available for the vortices to inject maximum momentum in the near wall region. In Fig.13 the micro-ramps were placed 17.3δ upstream of the incident shock. Therefore, if the micro-ramps are placed closer than $17.3\delta - 3.8\delta = 13.5\delta$ to the incident shock, a reduction in micro-ramp effectiveness may be expected. This is exactly what is noticed in Fig.9a. The average separated area remains relatively constant for $d > 13.8\delta$ and increases for $d < 13.8\delta$.

The boundary layer has now been investigated in terms of the wake intensity / location and the amount of momentum flux that is transported to the near-wall region. To relate these properties to the behaviour of the interaction region a technique called conditional averaging is used. The idea is to first sort the images based upon a certain condition, for instance boundary layer momentum flux. Then the images are grouped into two sets, one for which the images have a large value for the condition and another for which the values are small. By subtracting the 'small' from the 'large' set one can visualize the impact that the condition has on the flow field. In this analysis, images are grouped within the 'large' / 'small' set when their condition value is 1-3 standard deviations above / below the mean.

Fig.14 shows the differential U velocity fields for four different conditions. Fig.14(a) is conditioned on the boundary layer momentum flux in the near-wall region ($0 < 0.5\delta$). The higher speeds in the interaction region imply that one is likely to have a weaker separation bubble when the incoming boundary layer is rich in momentum. Furthermore, notice that also in the region of the reflected shock wave higher speeds are recorded. The reflected shock wave causes a deceleration of the flow, so higher values in this region imply a downstream displacement of the shock wave. So, when the boundary layer is rich in momentum, the reflected shock is likely to be displaced downstream. An observation that has also been made in the works of [19, 24].

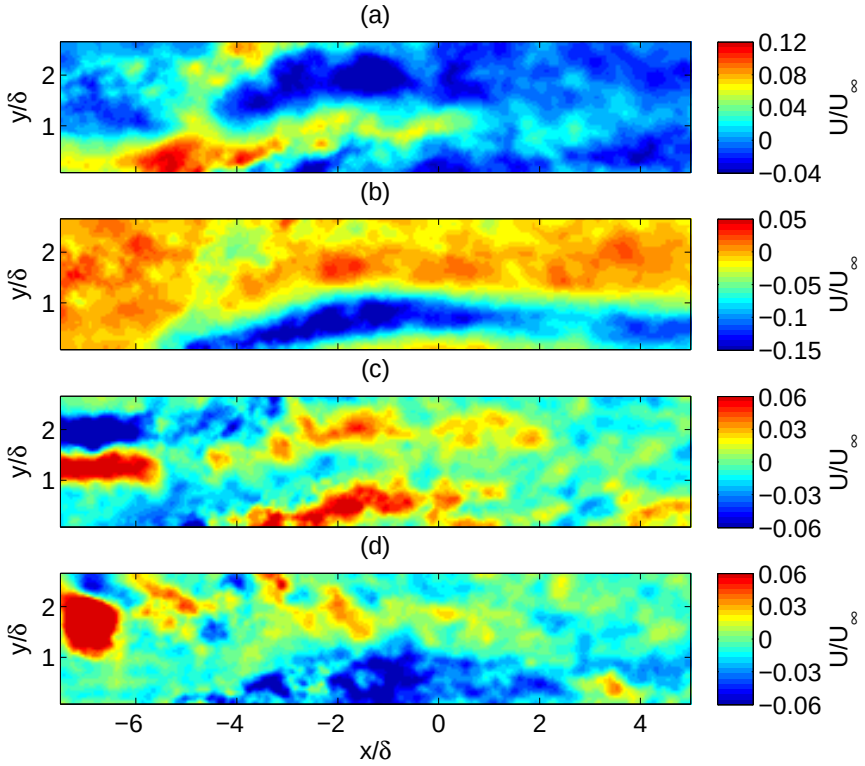

Figure 14: Results from conditional averaging, differential U velocity fields between large and small criterion events. Conditioned on (a) boundary layer momentum flux (b) size of the low-speed bubble (c) wake location (d) wake velocity

Fig.14(b) is conditioned on the size of the low-speed ($U < 0.2U_\infty$) bubble. Notice that the effect of the bubble size is not only felt in the interaction region, but is also clearly visible 5δ downstream of the incident shock. There is, however, no direct relation visible between bubble size and features of the incoming boundary layer. A similar observation was also made in the work of Van Oudheusden et al. [23], who employed the same technique on a shock wave boundary layer interaction without micro-ramp. They hypothesized that this might be due to an attenuated response of the bubble to the inflow conditions.

In the Figs.14(c) and (d) the effects of, respectively, the instantaneous wake location and speed are investigated. When the wake is entering the interaction relatively far away from the wall, one is likely to encounter a weaker separation bubble. The wake speed has the exact opposite effect, higher wake speeds appear to be correlated with a stronger separation bubble.

4. Conclusions

A planar PIV study has been carried out in order to quantify the effects of micro-ramp height and location on the separation probability of the flow and the reflected shock wave unsteadiness. Conditional averaging is used to show that the interaction is sensitive to the amount of momentum flux in the near-wall region ($<0.5\delta$) of the incoming boundary layer. The momentum flux that is added to this region scales linearly with micro-ramp height and is shown to increase upto 5.7δ downstream of the ramp. After 5.7δ a plateau is reached and virtually no extra momentum is added or lost. Therefore, if the distance between the micro-ramp's trailing edge and the foot of the reflected shock wave is less than 5.7δ, full boundary layer mixing is not attained and reduced performance is expected.

The measurements that were carried out on the interaction region indeed confirm this result. The average separated area is relatively constant for $d > 13.8\delta$ (micro-ramp and reflected shock wave are separated by 6.1δ) and increases when the micro-ramp is placed closer to the interaction. For the special case of a 4 mm micro-ramp placed 10.4δ upstream of the incident shock wave, there appears a very large region of reversed flow, multiple times larger than without a micro-ramp. This means that if micro-ramps are to be used in a supersonic jet inlet, it is important to maintain a certain minimum distance between the micro-ramp and the interaction during all flight regimes. The dependency of this minimum distance on Mach number and Reynolds number is still to be investigated.

The 3 and 4 mm micro-ramp are more effective in reducing the average shock-induced separated area than the 2 mm micro-ramp. The best performance is achieved with a 4 mm ramp located 20.8δ upstream of the interaction. For this particular case the average separated area is reduced by a factor of 20 in the centreline of the ramp. Larger micro-ramps are also more effective in reducing the reflected shock wave unsteadiness. A 4 mm micro-ramp ($d = 13.8\delta$) is able to reduce the shock unsteadiness by 53%. Although the larger micro-ramps perform better than the smaller micro-ramps, this does come at the price of a higher drag contribution.

At off-centreline locations the micro-ramp is less effective. If the measurement plane is aligned with the outer edge of the micro-ramp ($h = 4$ mm, $d = 17.3\delta$), the average separated area is measured to be 12% larger than for a clean configuration. The micro-ramp therefore does not remove separation completely, but instead creates a spanwise modulation in the bubble. The shock unsteadiness for the same case is, however, reduced by 36% compared to a clean configuration. It can be hypothesized that by breaking up the bubble in a cellular structure, the degrees of freedom of the reflected shock wave are reduced, consequently reducing the shock unsteadiness.

References

[1] D. S. Dolling. Fifty Years of Shock-Wave/Boundary-Layer Interaction Research: What Next? *AIAA Journal*, 39(8):1517–1531, August 2001.

[2] H. Babinsky and J. K. Harvey. *Shock Wave-Boundary-Layer Interactions*. Cambridge University Press, Cambridge, 2011.

[3] M. K. Fukuda, W. G. Hingst, and E. Reshotko. Control of Shock Wave - Boundary Layer Interactions by Bleed in Supersonic Mixed Compression Inlets. Technical report, NASA CR-2595, 1975.

[4] P. R. Ashill, J. L. Fulker, and K. C. Hackett. A Review of Recent Developments in Flow Control. *Aeronautical Journal*, 109(1095):205–232, 2005.

[5] D. C. McCormick. Shock/Boundary-Layer Interaction Control with Vortex Generators and Passive Cavity. *AIAA Journal*, 31(1):91–96, January 1993.

[6] J .W. Barter and D. S. Dolling. Reduction of Fluctuating Pressure Loads in Shock/Boundary-Layer Interactions using Vortex Generators. *AIAA Journal*, 33(10):1842–1849, October 1995.

[7] J. C. Lin. Review of research on low-profile vortex generators to control boundary-layer separation. *Progress in Aerospace Sciences*, 38(4-5):389–420, May 2002.

[8] H. Babinsky, Y. Li, and C. W. Pitt Ford. Microramp Control of Supersonic Oblique Shock-Wave/Boundary-Layer Interactions. *AIAA Journal*, 47(3):668–675, March 2009.

[9] B. H. Anderson, J. Tinapple, and L. Surber. Optimal Control of Shock Wave Turbulent Boundary Layer Interactions Using Micro-Array Actuation. In *3rd AIAA Flow Control Conference*, pages 1–14, San Francisco, California, 2006. AIAA 2006-3197.

[10] P. L. Blinde, R. A. Humble, B. W. van Oudheusden, and F. Scarano. Effects of micro-ramps on a shock wave/turbulent boundary layer interaction. *Shock Waves*, 19(6):507–520, September 2009.

[11] S. Lee, M. K. Goettke, E. Loth, J. Tinapple, and J. Benek. Microramps Upstream of an Oblique-Shock/Boundary-Layer Interaction. *AIAA Journal*, 48(1):104–118, January 2010.

[12] D. Ragni, F. F. J. Schrijer, B. W. van Oudheusden, and F. Scarano. Particle tracer response across shocks measured by PIV. *Experiments in Fluids*, 50(1):53–64, May 2010.

[13] M. Samimy and S. K. Lele. Motion of particles with inertia in a compressible free shear layer. *Physics of Fluids A: Fluid Dynamics*, 3(8):1915–1923, 1991.

[14] J. Westerweel and F. Scarano. Universal outlier detection for PIV data. *Experiments in Fluids*, 39(6):1096–1100, August 2005.

[15] Z. Sun, F. F. J. Schrijer, F. Scarano, and B. W. van Oudheusden. The three-dimensional flow organization past a micro-ramp in a supersonic boundary layer. *Physics of Fluids*, 24:1–22, 2012.

[16] D. Coles. The law of the wake in the turbulent boundary layer. *J. Fluid Mechanics*, 1:191–226, 1956.

[17] H. H. Fernholz and P. J. Finley. A Critical Commentary on Mean Flow Data for Two-Dimensional Compressible Turbulent Boundary Layers, 1980.

[18] P. S. Klebanoff. Characteristics of Turbulence in a Boundary Layer with Zero Pressure Gradient, 1955.

[19] R. A. Humble, G. E. Elsinga, F. Scarano, and B. W. van Oudheusden. Three-dimensional instantaneous structure of a shock wave/turbulent boundary layer interaction. *Journal of Fluid Mechanics*, 622:33, February 2009.

[20] M. Elene and J.-P. Lacharme. Experimental study of a supersonic turbulent boundary layer using a laser Doppler anemometer. *Journal de mécanique théorique et appliquée*, 7(2):175–190, 1988.

[21] L. J. Souverein. *On the scaling and unsteadiness of shock induced separation*. PhD thesis, Delft University of Technology, 2010.

[22] J.-P. Dussauge, P. Dupont, and J.-F. Debiève. Unsteadiness in shock wave boundary layer interactions with separation. *Aerospace Science and Technology*, 10(2):85–91, March 2006.

[23] B. W. Oudheusden, A. J. P. Jöbsis, F. Scarano, and L. J. Souverein. Investigation of the unsteadiness of a shock-reflection interaction with time-resolved particle image velocimetry. *Shock Waves*, 21(5):397–409, February 2011.

[24] B. Ganapathisubramani, N. T. Clemens, and D. S. Dolling. Effects of upstream boundary layer on the unsteadiness of shock-induced separation. *Journal of Fluid Mechanics*, 585:369–394, August 2007.